peak potentials for oxidation of the corresponding neutral monohydrides are linearly related by eq 22. It is not clear yet why the slope of the pK_a vs E_{pa} plots is −10.7 and not the −16.9 value predicted by theory.

When the contributions to the acidity of the dihydrogen and dihydride forms are factored out, the two forms give approximately the same pK_a vs E_{pa} equations (Figure 4). Thus, the dihydrogen ligand does not appear to have an acid/base chemistry distinct from that of dihydrides in this case. The thermodynamic acidity of the two tautomers just depends on relative amounts of the two forms. When the dihydride form is more abundant, as in the complexes $[CpRuH_2(L)]^+$, L = dppm, dppe, and dape, the dihydrogen form is more acidic, as reported previously.[21] However, for the more electron rich complexes $[CpRuH_2(dmpe)]^+$ and $[Cp^*RuH_2(dppm)]^+$, the dihydride form has a greater thermodynamic acidity. The kinetics of protonation/deprotonation of the dihydrogen and dihydride forms of the complexes remains to be determined so that any differences in the kinetic acidity can be detected.

Equation 22 can be used to predict that cyclopentadienylruthenium(II) dihydrogen complexes can have a wide range of pK_a values—from −6 to 12. This explains how dihydrogen gas (with $pK_a \sim 35$[52]) can be converted into a strong acid when it is coordinated to transition-metal ion. New chemical reactions of acidic dihydrogen complexes will be reported shortly.

Acknowledgment. This research was supported by grants to R.H.M. from the Natural Sciences and Engineering Research Council of Canada, by the donors of the Petroleum Research Fund, administered by the American Chemical Society, and by a loan of ruthenium chloride from Johnson Matthey Co. We thank the reviewers and Dr. Steven Simpson for useful comments.

(52) Buncel, E.; Menon, B. C. *J. Am. Chem. Soc.* **1977**, *99*, 4457-4461.

EXAFS Studies of Ni^{II}, Ni^{I}, and Ni^{I}–CO Tetraazamacrocycles and the Crystal Structure of (5,7,7,12,14,14-Hexamethyl-1,4,8,11-tetraazacyclotetradeca-4,11-diene)nickel(I) Perchlorate

Lars R. Furenlid,[1a] Mark W. Renner,[1a] David J. Szalda,[1b,c] and Etsuko Fujita*,[1c]

Contribution from the Department of Applied Science and Chemistry Department, Brookhaven National Laboratory, Upton, New York 11973. *Received July 19, 1990*

Abstract: Nickel(II) complexes of tetraazamacrocycles undergo one-electron reduction to produce either a nickel(I) complex or a nickel(II) anion radical. Both reduced species react with CO. The nature of the parent Ni(II) complexes, the reduced species, and the Ni^{I}–CO complexes were studied in CH_3CN by means of EXAFS and UV–vis spectroscopy to characterize structural differences as a function of oxidation state and axial ligation of the metal in solution. The EXAFS results reveal that the reduction of Ni(II) to Ni(I) results not only in an expansion of the macrocycle core (0.1 Å change in Ni–N bond distance) but also a distortion. On the other hand, the Ni(II) to Ni(II) anion radical reduction leaves the geometry around the nickel atom unchanged. The anion radical of Ni(II) tetraene$^+$ (NiL_3^+, L_3 = 2,3,9,10-tetramethyl-1,4,8,11-tetraazacyclotetradeca-1,3,8,10-tetraene) dimerizes in solution forming diamagnetic adducts. The monomer–dimer equilibrium constant was determined to be $K_1 = (5.5 \pm 1.0) \times 10^4\ M^{-1}$ from the electronic spectra. EXAFS data on CO adducts of $Ni^{I}L_1$, -L_2, and -L_3 (L_1 = 5,7,7,12,14,14-hexamethyl-1,4,8,11-tetraazacyclotetradeca-4,11-diene, L_2 = 5,7,7,12,12,14-hexamethyl-1,4,8,11-tetraazacyclotetradeca-4,14-diene) clearly indicate that these are five-coordinate complexes with a short Ni–C bond. Both $Ni–N_{imine}$ and $Ni–N_{amine}$ distances in the CO adducts of the Ni(I) complexes increase quite dramatically compared to those in the parent Ni(II) and Ni(I) complexes. The structure of the title nickel(I) complex has been determined from single-crystal X-ray diffraction data collected by using Mo Kα radiation. Crystallographic data are as follows: space group $P2/n$ with $a = 15.717$ (6) Å, $b = 8.196$ (2) Å, $c = 16.049$ (6) Å, $\beta = 100.67$ (3)°, $V = 2031$ (2) Å^3, $Z = 4$. The two square-planar nickel atoms in the asymmetric unit are situated on crystallographic inversion centers. The $Ni–N_{imine}$ distances are 1.988 (7) and 1.979 (7) Å and $Ni–N_{amine}$ distances are 2.063 (6) and 2.068 (6) Å, which are in good agreement with the EXAFS data.

Introduction

Factor 430 (**1**) is a nickel(II) hydrocorphin and the prosthetic group of methyl coenzyme M reductase. It catalyzes the reductive cleavage of *S*-methyl coenzyme M to coenzyme M and methane in the final step of the reduction of carbon dioxide to methane in methanogenic bacteria.[2] The structure of the pentamethyl ester derivative (F430M) has been determined by a combination of biosynthetic and NMR spectroscopic methods,[3]

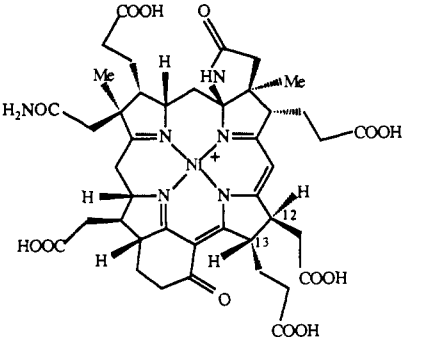

1

Although the detailed function of F430 is not known, an ESR signal detected[4] in suspensions of whole cells of *Methanobacterium thermoautotrophicum* was attributed to the active site and in-

(1) (a) Department of Applied Science. (b) Permanent address: Department of Natural Sciences, Baruch College, Manhattan, NY 10010. (c) Chemistry Department.

(2) (a) Gulsalus, R. P.; Wolfe, R. S. *J. Bacteriol.* **1978**, *135*, 851. (b) Ellefson, W. L.; Whitman, W. B.; Wolfe, R. S. *Proc. Natl. Acad. Sci. U.S.A.* **1982**, *79*, 3707. (b) Livingston, D. A.; Pfaltz, A.; Schreiber, J.; Eschenmoser, A.; Ankel-Fuchs, D.; Moll, J.; Jaenchen, R.; Thauer, R. K. *Helv. Chim. Acta* **1984**, *67*, 334. (c) Fässler, A.; Kobelt, A. Pfaltz, A.; Eschenmoser, A.; Bladon, C.; Battersby, A. R.; Thauer, R. K. *Helv. Chim. Acta* **1985**, *68*, 2287. (d) Daniels, L.; Sparling, R.; Sprott, G. D. *Biochem. Biophys.* **1984**, *768*, 113.

(3) (a) Pfaltz, A.; Jaun, B.; Fässler, A.; Eschenmoser, A.; Jaenchen, R.; Gilles, H.; Diekert, G.; Thauer, R. K. *Helv. Chim. Acta* **1982**, *65*, 828. (b) Won, H.; Olson, K. D.; Wolfe, R. S.; Summers, M. F. *J. Am. Chem. Soc.* **1990**, *112*, 2178.

(4) (a) Albracht, S. P. J.; Ankel-Fuchs, D.; Van der Zwaan, J. W.; Fontijn, R. D.; Thauer, R. K. *Biochim. Biophys. Acta* **1986**, *870*, 57. (b) Albracht, S. P. J.; Ankel-Fuchs, D.; Böcher, R.; Ellerman, J.; Moll, J.; Van der Zwaan, J. W.; Thauer, R. K. *Biochim. Biophys. Acta* **1988**, *86*, 955.

0002-7863/91/1513-883$02.50/0

terpreted as the nickel ion of F430 in a monovalent or trivalent oxidation state. Isolated F430M has been reduced reversibly from the Ni(II) to the Ni(I) form in THF, and the latter has been characterized by UV–vis and ESR spectroscopy.[5] Although the in vivo ESR spectrum indicates more pronounced axial anisotropy, the g values and hyperfine couplings in both ESR spectra were consistent with a Ni(I) ion with four equivalent N atoms in the equatorial plane. It has been also shown[6] that the Ni(I) form of F430M is an efficient catalyst for the reductive cleavage of methyl sulfonium salts to methane and thio ethers. Recent studies have demonstrated[7] that native F430 shows thermal degradation to form two other stereoisomers (13-monoepimer and the more stable 12,13-diepimer). X-ray absorption studies[8] show that native F430 is six-coordinate with long nickel(II)–ligand distances (~2.1 Å), suggesting a high-spin nickel. (The nature of the axial ligands in F430 is unidentified yet.) In contrast, the 12,13-diepimer has a four-coordinate, square-planar structure with short nickel(II)–nitrogen bonds (~1.9 Å), suggesting a ruffled conformation and considerable flexibility of the macrocycle. The structural changes associated with the reduction of F430 are not known. (See Note Added in Proof.)

Despite the intense interest in CO_2 fixation and utilization, the reduction chemistry of Ni porphyrins and hydroporphyrins as models for F430 has only recently received attention.[9] Recent EXAFS studies[10] have shown that reduction of low-spin Ni(II) chlorin[11] and porphycene[11] results in the formation of Ni(II) π anion radicals with no observable structural changes. In contrast to this, the reduction of Ni^{II}iBC[11] yields a Ni(I) complex, and EXAFS data indicate that reduction induces a distortion in the macrocycle core rather than a simple expansion.

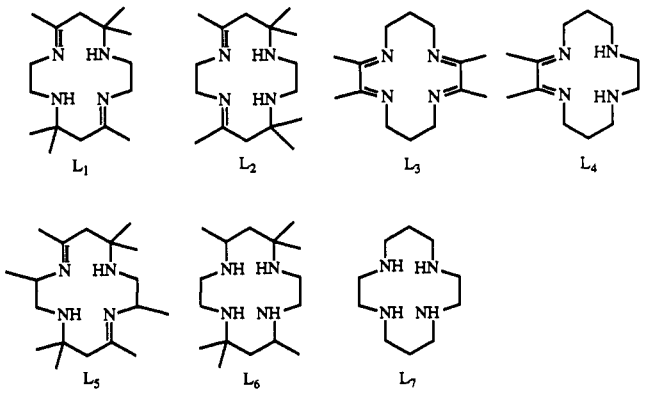

Since Curtis' template synthesis[12] of $[Ni^{II}L_1]^{2+}$, many 14-membered tetraazamacrocyclic complexes have shown interesting properties as catalysts for H_2O[13a] and CO_2[13b] reduction. Lovecchio et al.[14] studied the redox behavior of Ni macrocycles and found that Ni(II) complexes of all the above ligands except L_3 and L_4 form Ni(I) complexes upon one-electron reduction. Gagné et al.[15] determined CO binding constants in DMF for various Ni(I) macrocycles and several Ni(II) anion radicals including NiL_3^+. Intermediate formation of an alkyl–Ni(II) species has been postulated[16] for the reaction of Ni(I) tetraazamacrocycles with n-alkyl halides. As models of F430 and as an extension of previous work[17] on carbon dioxide activation by cobalt(I) macrocycles, we studied the EXAFS of Ni(II), Ni(I), or Ni(II) anion radical complexes of L_1, L_2, and L_3 and the CO adducts of the reduced species in CH_3CN to characterize the structural differences as a function of oxidation state and axial ligation of the metal in solution. In the course of this work, we obtained good crystals of $[Ni^IL_1]ClO_4$. We describe the crystal and molecular structure of $[Ni^IL_1]ClO_4$ and its comparison with the EXAFS data.

Experimental Section

Materials. The complexes $[Ni^{II}L_1](ClO_4)_2$ (L_1 = 5,7,7,12,14,14-hexamethyl-1,4,8,11-tetraazacyclotetradeca-4,11-diene), $[Ni^{II}L_2](ClO_4)_2$ (L_2 = 5,7,7,12,12,14-hexamethyl-1,4,8,11-tetraazacyclotetradeca-4,14-diene), $[Ni^{II}L_3](ClO_4)_2$ (L_3 = 2,3,9,10-tetramethyl-1,4,8,11-tetraazacyclotetradeca-1,3,8,10-tetraene), $[Ni^{II}L_4](ClO_4)_2$ (L_4 = 2,3-dimethyl-1,4,8,11-tetraazacyclotetradeca-1,3-diene), $[Ni^{II}L_6](ClO_4)_2$ (L_6 = 5,7,7,12,14,14-hexamethyl-1,4,8,11-tetraazacyclotetradecane), and $[Ni^{II}L_7](ClO_4)_2$ (L_7 = 1,4,8,11-tetraazacyclotetradecane) were prepared as previously described[14,18] and characterized by UV–vis, IR, and NMR spectroscopy. Analyses for nickel and perchlorate anion were satisfactory. (**Warning**: The perchlorate salts used in this study may be explosive and potentially hazardous.) CH_3CN and C_3H_7CN were purified according to published procedures[19] and stored under vacuum over activated molecular sieves (3Å) or CaH_2. Research grade CO (>99.997% pure) was used without further purification.

Spectroscopic Measurements. Measurements of the Ni(I) complexes and Ni(II) anion radicals required rigorous exclusion of oxygen and water.

UV–vis spectra were measured on a Cary 17 or Cary 210 spectrometer. The reduced species (3×10^{-5} to 8×10^{-3} M solutions) were made under vacuum by sodium amalgam (Na–Hg, 0.5% Na in Hg) reduction in sealed glassware equipped with an optical cell. Carbon monoxide complexes were prepared by the introduction of CO into the corresponding Ni(I) complexes. Molar absorptivities of all Ni(I) complexes assume 100% conversion from Ni(II) complexes.

IR measurements of the Ni(I)–CO complexes were made with ca. 7 mM CH_3CN solutions prepared similarly and transferred by syringe to a vacuum-tight IR cell (0.5 mm pathlength) which had been flushed with CO. The spectra were immediately measured on a Nicolet MX-1 or Mattson Polaris FT-IR spectrometer.

EXAFS experiments were carried out in vessels of published design[20] equipped with side arms for chemical reduction and UV–vis spectroscopy. In a typical preparation, a Ni(II) macrocycle sample was added to a cell which in turn was attached to a vacuum line and evacuated. Dry, degassed acetonitrile (~1 mL) was distilled in to produce 10–20 mM solutions. For measurements on the Ni(II) parent complexes, the solutions were simply transferred into the EXAFS arm without further treatment. Reduced species were generated by transferring the Ni(II) solution into the reduction arm to contact Na–Hg and following the extent of the reduction optically. Carbon monoxide adducts were pro-

(5) Jaun, B.; Pfaltz, A. *J. Chem. Soc., Chem. Commun.* **1986**, 1327.
(6) Jaun, B.; Pfaltz, A. *J. Chem. Soc., Chem. Commun.* **1988**, 293.
(7) Pfaltz, A.; Livingston, D. A.; Jaun, B.; Diekert, G.; Thauer, R. K.; Eschenmoser, A. *Helv. Chim. Acta* **1985**, *68*, 1338.
(8) Shiemke, A. K.; Hamilton, C. L.; Scott, R. A. *J. Biol. Chem.* **1988**, *263*, 5611.
(9) (a) Stolzenberg, A. M.; Glazer, P. A.; Foxman, B. M. *Inorg. Chem.* **1986**, *25*, 983. (b) Stolzenberg, A. M.; Stershic, M. T. *J. Am. Chem. Soc.* **1988**, *110*, 6391. (c) Stolzenberg, A. M.; Stershic, M. T. *Inorg. Chem.* **1987**, *26*, 1970. (d) Stolzenberg, A. M.; Stershic, M. T. *J. Am. Chem. Soc.* **1988**, *110*, 5397. (e) Lexa, D.; Momenteau, M.; Mispelte, J.; Savéant, J.-M. *J. Am. Chem. Soc.* **1989**, *111*, 30. (f) Renner, M. W.; Forman, A.; Fajer, J.; Simpson, D.; Smith, K. M.; Barkigia, K. M. *Biophys. J.* **1988**, *53*, 277. (g) Kadish, K. M.; Sazan, D.; Lin, Y. M.; Saoiabi, A.; Ferhat, M.; Guilard, R. *Inorg. Chem.* **1988**, *27*, 686. (h) Kadish, K. M.; Sazan, D.; Lin, Y. M.; Saoiabi, A.; Ferhat, M.; Guilard, R. *Inorg. Chem.* **1988**, *27*, 1198. (i) Chang, D.; Malinski, T.; Ulman, A.; Kadish, K. M. *Inorg. Chem.* **1984**, *23*, 817.
(10) Furenlid, L. R.; Renner, M. W.; Smith, K. M.; Fajer, J. *J. Am. Chem. Soc.* **1990**, *112*, 1634.
(11) Abbreviation of the compounds in this paper are as follows: chlorin, anhydromesorhodochlorin XV methyl ester; iBC, ring C of the chlorin also saturated. (See: Smith, K. M.; Simpson, D. J. *J. Am. Chem. Soc.* **1987**, *109*, 6326) porphycene, 2,7,12,17-tetrapropylporphycene. (See: Renner, M. W.; Forman, A.; Wu, W.; Chang, C. K.; Fajer, J. *J. Am. Chem. Soc.* **1989**, *111*, 8618) TPP, *meso*-tetraphenylporphyrin; OEP, octaethylporphyrin.
(12) (a) Curtis, N. F. *J. Chem. Soc.* **1960**, 4409. Curtis, N. F.; Curtis, Y.; Powell, H. K. J. *J. Chem. Soc. (A)* **1966**, 1015. (b) Curtis, N. F. *Coord. Chem. Rev.* **1968**, *3*, 3.
(13) (a) Brown, G. M.; Brunschwig, B. S.; Creutz, C.; Endicott, J. F.; Sutin, N. *J. Am. Chem. Soc.* **1979**, *101*, 1298. (b) Fisher, B.; Eisenberg, R. *J. Chem. Soc.* **1980**, *102*, 7361.
(14) Lovecchio, F. V.; Gore, E. S.; Busch, D. H. *J. Am. Chem. Soc.* **1974**, *96*, 3109.
(15) (a) Gagné, R. R.; Ingle, D. M. *J. Am. Chem. Soc.* **1980**, *102*, 1444. (b) Gagné, R. R.; Ingle, D. M. *Inorg. Chem.* **1981**, *20*, 420.
(16) (a) Godson, C.; Healy, K. P.; Pletcher, D. *J. Chem. Soc. Trans.* **1978**, 972. (b) Bakac, A.; Espenson, J. H. *J. Am. Chem. Soc.* **1986**, *108*, 713. (c) Ram, M. S.; Bakac, A.; Espenson, J. H. *Inorg. Chem.* **1986**, *25*, 326.
(17) (a) Fujita, E.; Szalda, D. J.; Creutz, C.; Sutin, N. *J. Am. Chem. Soc.* **1988**, *110*, 4870. (b) Fujita, E.; Creutz, C.; Sutin, N.; Szalda, D. J. *J. Am. Chem. Soc.* In press.
(18) Douglas, B. E. Editor-in Chief, *Inorganic Syntheses*; Wiley: New York, Vol. XVIII, 1978, references cited in ref 14.
(19) Riddick, J. A.; Bunger, W. B.; Sakano, T. K. *Organic Solvents, Physical Properties and Methods of Purification*; Wiley: New York, 1986.
(20) Furenlid, L. R.; Renner, M. W.; Fajer, J. *Rev. Sci. Instrum.* **1990**, *61*, 1326.

Table I. Experimental Details of the X-ray Diffraction Study of $[Ni^{I}L_1]ClO_4$

mol formula	$[Ni(N_4C_{16}H_{32})]ClO_4$
a, Å	15.717 (6)
b, Å	8.196 (2)
c, Å	16.049 (6)
β, deg	100.67 (3)
V, Å^3	2031 (2)
Z	4
mol wt	438.6
space group	$P2/n$
δ(calc), g cm^{-3}	1.43
radiation	Mo Kα (graphite monochromatized)
μ, cm^{-1}	11.14
transmission coefficients	
max	0.76511
min	0.67024
R	0.073
R_w	0.086
max shift/error, final cycle	less than 0.02
temp, K	294

duced by charging the cells with approximately 0.95 atm of CO. The NiL_3CO^+ sample was prepared in CH_3CN/C_3H_7CN (v/v = 1/5) and measured at 300 and 173 K; all other samples were measured at 300 K. Sample purity was verified spectroscopically before and after X-ray exposure.

X-ray absorption spectra were collected in fluorescence mode at Beam Line X-9A at the National Synchrotron Light Source. A geometrically efficient, cylindrical ionization chamber equipped with a cold gas temperature controller was used to collect 5–15 20-min scans of each sample in order to acquire $>10^6$ total counts of integrated signal. Ni^{II}cyclamI_2, for which a published crystal structure[21] is available, was measured in transmission mode as an EXAFS standard. Quantitative comparison with other previously measured, well-characterized nickel complexes, including Ni^{II}OEP and Ni^{II}porphycene, established internal consistency.[10] Individual data scans were inspected manually to remove any monochromator glitches, evident as spurious changes in I_0. Complete scans were then summed to form average spectra.

The EXAFS oscillations were isolated with standard techniques:[22] subtraction of a linear pre-edge baseline, normalization of the edge step, interpolation onto a photoelectron momentum grid, and subtraction of a smoothly varying absorption background with a three- or four-segment cubic spline. Resulting χ oscillations were weighted with k^3 and Fourier filtered with Hanning windows to recover first-shell EXAFS. Quantitative comparison between standard and unknowns was accomplished with nonlinear least-squares fitting and ratio techniques.[23] It is assumed that the EXAFS oscillations are described by

$$\chi(k) = \sum_j A_j(k) \sin(2kr_j + \phi_j(k))$$

$$A_j(k) = [N_j S_i(k) F_j(k)/kr_j^2] \exp(-2\sigma_j^2 k^2) \exp(-2r_j/\lambda(k))$$

$$k = 2\pi[2m_e(E - E_0)]^{1/2}/h$$

where k is the electron momentum vector, E is the incident photon energy, E_0 is the threshold energy of that particular absorption edge, r_j is the radial distance to the jth atom, $F_j(k)$ is the backscattering amplitude from each of the N_j neighboring atoms of the jth type with a Debye–Waller type factor of σ_j, and ϕ_j is the total phase shift experienced by the photoelectron. The term $\exp(-2r_j/\lambda)$ is due to inelastic losses in the scattering process with λ an effective electron mean free path. $S_i(k)$ is an amplitude reduction factor due to many-body effects at the central atom (denoted by i). All terms except N, r, and σ are assumed transferable between standards and unknowns.

Binding Constant Measurements. CO binding constants were determined by previously described cyclic voltammetry techniques.[24,25] Cyclic voltammograms were obtained on a BAS100 electrochemical analyzer with scan rates ranging from 2 to 25 mV s^{-1} using a conventional H-type cell. Solutions contained 1 mM nickel complex and 0.1 M tetrapropylammonium perchlorate in dry CH_3CN and gas compositions of 0, 20, 50, and 100% CO in Ar. Graphite, Pt, and SCE were used as working, counter, and reference electrodes, respectively. Ferrocene was used as an internal standard. The solubility of CO in CH_3CN at 25 °C was previously determined to be 0.0083 M.[17b]

Table II. Selected Bond Distances and Angles in $[Ni^{I}L_1]ClO_4$

	molecule 1	molecule 2
	Distances, Å	
Ni–N1	2.063 (6)	2.068 (6)
Ni–N4	1.988 (7)	1.979 (7)
	Angles, deg	
N1–Ni–N4	85.0 (3)	85.6 (3)
N1–Ni–N4′	95.0 (3)	94.4 (3)

Collection and Reduction of X-ray Data. $[Ni(N_4C_{16}H_{32})]ClO_4$, NiL_1ClO_4, crystallized as deep red prisms from CH_3CN at room temperature by the slow removal of the solvent under vacuum. The air-sensitive crystals were coated with petroleum jelly and mounted in a glass capillary. A crystal with the dimensions of 0.32 × 0.30 × 0.50 mm^3 was used for data collection. An X-ray study of the crystals revealed monoclinic symmetry with systematic absences $h0l$, $h + l = 2n + 1$, which is consistent with the space group Pn (a nonstandard setting of space group Pc) or $P2/n$ (a nonstandard setting of space group $P2/c$).[26a] Crystal data and complete details of data collection and reduction are provided in Table I and Table S1 (supplementary material).

Determination and Refinement of Structure. E statistics indicated a centrosymmetric space group. The structure was solved by the calculation of a Patterson map[27] which indicated the presence of two nickel atoms and two chlorine atoms in the asymmetric unit, each nickel atom being situated on a crystallographic inversion center and each chlorine atom lying on a special position having 2-fold symmetry. The $Ni^{I}L_1^+$ ion contains a center of inversion which is consistent with the ligand being the meso isomer. A series of difference Fourier maps[27] were used to locate the remaining atoms in the asymmetric unit. All non-hydrogen atoms were refined with anisotropic thermal parameters, while the hydrogen atoms were placed at calculated positions (X–H = 0.95 Å) and allowed to "ride" on the atom to which they were attached. A common isotropic temperature parameter for all the hydrogen atoms was included in the refinement (U = 0.079 (6)). The quantity $\sum w(|F_o| - |F_c|)^2$ was minimized during the least-square refinements with use of neutral atom scattering factors[26b] and anomalous dispersion effects.[26c]

Final non-hydrogen atomic positional parameters are given in Table S2, and selected interatomic distances and angles are listed in Table II. A listing of observed and calculated structure factors is given in Table S3, and the final thermal parameters for the non-hydrogen atoms are provided in Table S4. The calculated hydrogen atom positions are listed in Table S5. A complete listing of all interatomic bond distances and angles is provided in Table S6. Distances and angles of proposed hydrogen bonds are shown in Table S7. (Tables S1–S7 are deposited as supplementary material.)

Extended Hückel Calculations. Charge iterative extended Hückel calculations were carried out with previously described.[28] programs and parameters. The atomic coordinates for $Ni^{II}L_1^{2+}$ and $Ni^{I}L_1^+$ complexes were taken from the published[29] and current crystallographic data, respectively. Coordinates for $Ni^{I}L_1CO^+$ and $Ni^{II}L_3^{2+}$ were assumed to be the same as those of the corresponding cobalt complexes.[30,31] The structure of the anion radical, $Ni^{II}L_3^+$, was assumed to be same as the $Ni^{II}L_3^{2+}$ parent complex.

Results

Near-Edge Structure. Features in the nickel near-edge absorption spectrum reflect the ligation geometry around the metal

(21) Prasad, L.; McAuley, A. *Acta Crystallogr.* **1983**, *C39*, 1175.
(22) (a) Stern, E. A.; Heald, S. M. *Handbook on Synchrotron Radiation*; Koch, E. E., Ed.; North Holland: Amsterdam, 1983. (b) Teo, B. K. *EXAFS: Basic Principles and Data Analysis*; Springer-Verlag: Berlin, Heidelberg, New York, Tokyo, 1986, and references cited therein.
(23) Bunker, G. B. *Nucl. Inst. Meth.* **1983**, *207*, 437.
(24) Bard, A. J.; Faulkner, L. R. *Electrochemical Methods, Fundamentals and Application*; John Wiley & Sons, Inc.: New York, 1980; p 34.
(25) Gagné, R. R.; Allison, J. L.; Inble, D. M. *Inorg. Chem.* **1979**, *18*, 2767.
(26) (a) *International Tables for X-ray Crystallography*, 3rd ed.; Kynoch Press: Birmingham, England, 1969; Vol. I, pp 74–75. (b) *International Tables for X-ray Crystallography*; Vol. IV, pp 99–101 and 149–150. (c) Cromer, D. T.; Liberman, D. *J. Chem. Phys.* **1970**, *53*, 1891.
(27) SHELX-76: Sheldrick, G. M. In *Computing in Crystallography*; Shenk, H., Olthof-Hazekamp, R., van Koningsveld, H., Bassi, G. C., Eds.; Delft University: Delft, Holland, 1978; pp 34–42.
(28) (a) Davis, M. S.; Forman, A.; Hanson, L. K.; Thornber, J. P.; Fajer, J. *J. Phys. Chem.* **1979**, *83*, 3325. (b) Chang, C. K.; Hanson, L. K.; Richardson, P. F.; Young, R.; Fajer, J. *Proc. Natl. Acad. Sci. U.S.A.* **1981**, *78*, 2652. (c) Zerner, M.; Gouterman, M. *Theor. Chim. Acta* **1966**, *4*, 44.
(29) Bailey, M. F.; Maxwell, I. E. *J. Chem. Soc., Dalton Trans.* **1972**, 938.
(30) Szalda, D. J.; Fujita, E.; Creutz, C. *Inorg. Chem.* **1989**, *28*, 1446.
(31) Endicott, J. F.; Lilie, J.; Kuszaj, J. M.; Ramaswamy, B. S.; Schmonsees, W. G.; Simic, M. G.; Glick, M. D.; Rillema, D. P. *J. Am. Chem. Soc.* **1977**, *99*, 429.

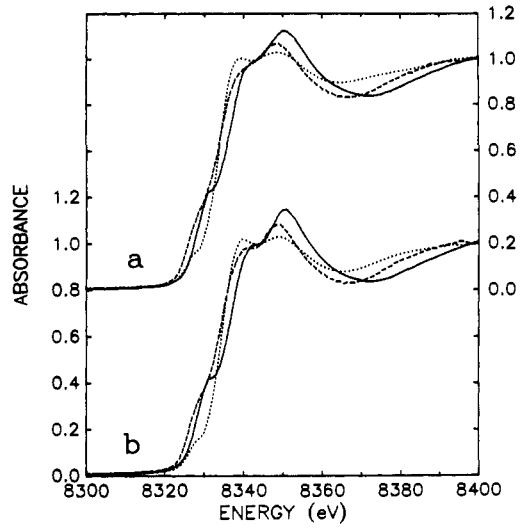

Figure 1. (a) Near-edge structures for NiL_1 complexes in CH_3CN: solid line $Ni^{II}L_1^{2+}$, broken line $Ni^{I}L_1^{+}$, dotted line $Ni^{I}L_1CO^{+}$. (b) Near-edge structures for NiL_2 complexes in CH_3CN: solid line $Ni^{II}L_2^{2+}$, broken line $Ni^{I}L_2^{+}$, dotted line $Ni^{I}L_2CO^{+}$.

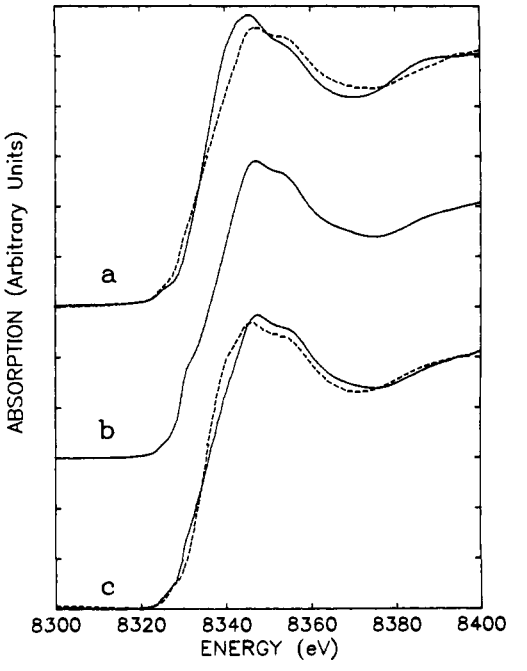

Figure 2. Near-edge structures for NiL_3 complexes: (a) solid line, six-coordinate $Ni^{II}L_3^{2+}$ in CH_3CN; broken line, four-coordinate $Ni^{II}L_3^{2+}$ in CH_3NO_2, (b) four-coordinate $Ni^{II}L_3^{+}$ in CH_3CN, and (c) NiL_3CO^{+} in CH_3CN/C_3H_7CN (v/v = 1/5) under 720 Torr CO, solid line, 300 K; broken line, 173 K.

in an unambiguous manner. Previous work[32] has shown that the intensity of a pre-edge absorption peak approximately 6 eV below the main edge, assigned as a $1s\text{-}4p_z$ type of electronic transition, directly correlates with the nickel coordination number when the nickel is four-, five-, or six-coordinate. A five-coordinate or a four-coordinate tetrahedral geometry further displays an enhanced 1s–3d absorption "pip" due to mixing of p character into the 3d molecular orbitals as a result of the loss of inversion symmetry.[33a] As is clearly evident from the edge plots in Figure 1, $Ni^{II}L_1^{2+}$, $Ni^{I}L_1^{+}$, $Ni^{II}L_2^{2+}$, and $Ni^{I}L_2^{+}$ show the pre-edge absorption features associated with four-coordinate, planar geometries, $Ni^{I}L_1CO^{+}$ and $Ni^{I}L_2CO^{+}$ have the attenuated pre-edge absorption associated with five-coordinate ligation geometry. The near-edge structure of $Ni^{II}L_3^{2+}$ shown in Figure 2a was solvent dependent: six-coordinate in CH_3CN (solid line) and four-coordinate in CH_3NO_2 (broken line). The reduced species, $Ni^{II}L_3^{+}$, is clearly four-coordinate in CH_3CN, Figure 2b. The edge of NiL_3CO^{+} (Figure 2c) in CH_3CN/C_3H_7CN (v/v = 1/5) at 300 K (solid line) is complicated, consistent with the existence of an equilibrium mixture of monomer $Ni^{II}L_3^{+}$, its dimer (see below), and $Ni^{I}L_3CO^{+}$. At 173 K (broken line), the pre-edge clearly has the structure associated with five-coordinate NiL_3CO^{+}. This observation is supported by the optical spectra (see Figure 7) of NiL_3CO^{+} in C_3H_7CN under 720 Torr of CO at various temperatures.

Numerous efforts to correlate metal oxidation state with K-shell absorption edge features have been made for transition metals. It has been shown[33b] with both theoretical and experimental studies that while the charge state of the absorbing atom directly affects

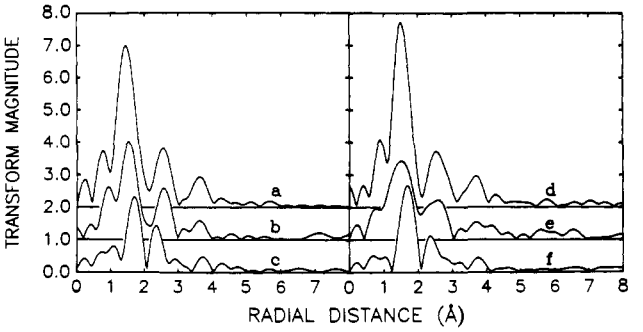

Figure 3. Fourier transforms of k^3 weighted EXAFS in CH_3CN: (a) $Ni^{II}L_1^{2+}$, (b) $Ni^{I}L_1^{+}$, (c) $Ni^{I}L_1CO^{+}$, (d) $Ni^{II}L_2^{2+}$, (e) $Ni^{I}L_2^{+}$, (f) $Ni^{I}L_2CO^{+}$.

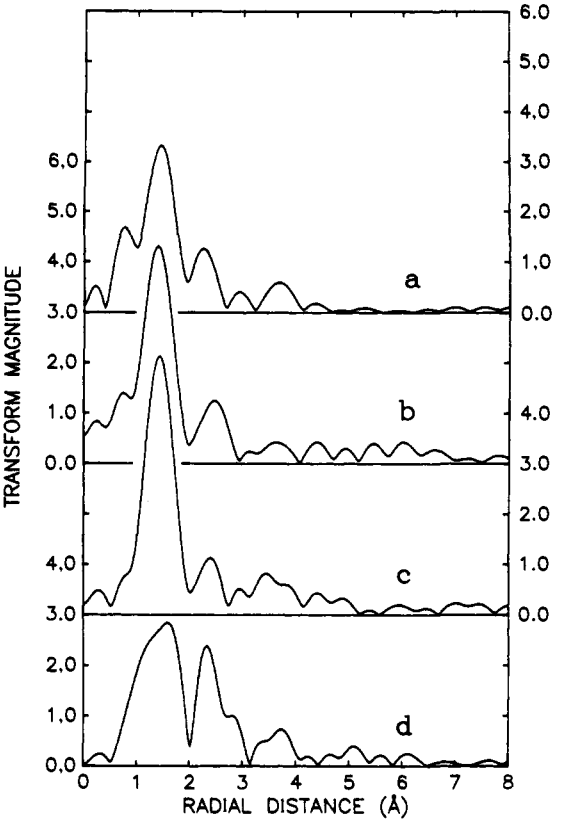

Figure 4. Fourier transforms of k^3 weighted EXAFS for NiL_3 complexes: (a) six-coordinate $Ni^{II}L_3^{2+}$ in CH_3CN, (b) four-coordinate $Ni^{II}L_3^{2+}$ in CH_3NO_2, (c) four-coordinate $Ni^{II}L_3^{+}$ in CH_3CN, (d) $Ni^{I}L_3CO^{+}$ in CH_3CN/C_3H_7CN (v/v = 1/5) at 173 K under 720 Torr CO.

(32) (a) Eidsness, M. K.; Sullivan, R. J.; Schwartz, J. R.; Hartzell, P. L.; Wolfe, R. S.; Flank, A.-M.; Cramer, S. P.; Scott, R. A. *J. Am. Chem. Soc.* **1986**, *108*, 3120. (b) Shiemke, A. K.; Kaplan, W. A.; Hamilton, C. L.; Shelnutt, J. A.; Scott, R. A. *J. Biol. Chem.* **1989**, *264*, 7276.

(33) (a) Bunker, G.; Stern, E. A.; Blankenship, R. E.; Person, W. *Biophys. J.* **1982**, *37*, 539. (b) Bunker, G. Ph.D. Thesis, University of Washington, 1984.

Table III. Near-Edge Results[a,b] for Various Ni Complexes in Acetonitrile at 300 K

complex	coordination no.	edge shift, eV
$[Ni^{II}L_1](ClO_4)_2$	4	0.0
$[Ni^{II}L_2](ClO_4)_2$	4	0.0
$[Ni^{II}L_3](ClO_4)_2$	6	
$[Ni^{II}L_3](ClO_4)_2$[c]	4	
$[Ni^{I}L_1]ClO_4$	4	−3.0
$[Ni^{I}L_2]ClO_4$	4	−2.0
$[Ni^{II}L_3]ClO_4$	4	
$[Ni^{I}L_1CO]ClO_4$	5	−1.5
$[Ni^{I}L_2CO]ClO_4$	5	−0.5
$[Ni^{I}L_3CO]ClO_4$[d]	5	

[a] Edge shift are measured at midpoint of edge step in comparison to $[Ni^{II}L_1](ClO_4)_2$. [b] Coordination number is estimated qualitatively from $4p_z$ transitions and 3d pips. [c] In CH_3NO_2. [d] In CH_3CN/C_3H_7CN (v/v = 1/5) at 173 K.

the edge energy, other parameters, such as changes in bond lengths, also influence the edge position and make it difficult, in most cases, to accurately assign an oxidation state from edge spectra alone. Nonetheless, a general trend of higher oxidation states having higher edge energies has been noted. Table III lists the edge midpoint energies for the Ni complexes. Upon reduction to Ni(I), the edges shift downward by 2–3 eV. Addition of CO results in a shift back toward the Ni(II) position by ~1.5 eV.

EXAFS. Fourier transforms of k^3 weighted EXAFS of the Ni(II) parent complexes, their one-electron reduction products, and their CO adducts are displayed in Figures 3 and 4. Both NiL_1 and NiL_2 complexes can be seen to undergo dramatic changes in the first-shell coordination upon reduction to form Ni(I) and further changes upon the addition of CO. The attenuation of the first-shell peak in the transform which occurs upon reduction immediately suggests an increase in the disorder factors. Coordination of CO results in even smaller first-shell amplitudes and suggests even greater distortion in the nickel coordination environment. In contrast, the Fourier transform of the EXAFS of anion radical, $Ni^{II}L_3^+$ (Figure 4c), does not show significant differences from the parent complex in CH_3NO_2 (Figure 4b). The $Ni^{II}L_3^{2+}$ complex (Figure 4a) in CH_3CN, which appears to be six-coordinate from the absorption edge, has a smaller transform amplitude than the four-coordinate species (Figure 4b,c), again suggesting multiple distances in the first-shell. The $Ni^{I}L_3CO^+$ complex (Figure 4d) again shows a reduced first-shell amplitude as noted for $Ni^{I}L_1CO^+$ and $Ni^{I}L_2CO^+$ (Figure 3c,f) and is interpreted as a disordered environment.

Quantitative results from nonlinear least-squares fitting are presented in Table IV and bear out the qualitative interpretation of increased disorder in the reduced species. The solution EXAFS results for both the $Ni^{II}L_1$ and $-L_2$ complexes in CH_3CN and $Ni^{II}L_3$ in CH_3NO_2 each indicate four approximately equal Ni–N bond lengths and small difference Debye–Waller factors. On the other hand, the EXAFS of $Ni^{II}L_3^{2+}$ in CH_3CN failed to fit with a coordination number of four. The NMR spectrum of $Ni^{II}L_3^{2+}$ in CD_3CN indicates the existence of a paramagnetic species, in agreement with a high-spin and six-coordinate nickel complex. A good fit was obtained by a six-coordinate model; four Ni–N bond distances of 1.96 Å and two Ni–axial ligand distances of 2.17 Å.

Single-shell fits for the $Ni^{I}L_1$ and $-L_2$ complexes show large Debye–Waller factors. Acceptable fits were obtained with the first-shell split into two distinct metal–nitrogen distances. In each case, comparison with the corresponding Ni(II) complex shows two bond distances remain approximately unchanged, while the other two lengthen by ~0.14 Å. With the two-shell fits, difference Debye–Waller factors are again reasonable. Some correlation of distances with selection of E_0 was noted, and Table IV lists fits with and without a 5-eV shift. The $Ni^{II}L_3^+$ anion radical yields four Ni–N bonds of 1.88 Å, the same as for the $Ni^{II}L_3$ parent complex in CH_3NO_2.

Analysis of the CO adducts was complicated by the lack of a Ni–C standard. However, since it is in general difficult to distinguish between C and N backscatterers, the data were analyzed as if the first-shells contained five nitrogens. This undoubtedly increases the uncertainties in the EXAFS parameters extracted. No acceptable fits were obtained with a single-shell model. For CO adducts of NiL_1^+ and NiL_2^+, fits using a two-distance model converged with a single short bond, presumably Ni–C, and four longer bonds, with large Debye–Waller factors for the latter. Therefore the final fits consist of a three-shell model with two types of nitrogens as well as the short Ni–C bond. In contrast, for the CO adduct of NiL_3^+ a model with one short Ni–C bond and four longer Ni–N bonds was adequate. All Ni–N distances are substantially longer than in the starting Ni(II) cases, consistent with the nickel moving out of the plane of the coordinating nitrogen atoms upon binding of CO. No EXAFS contributions from scattering by the CO oxygen are unambiguously evident in the Fourier transforms in Figures 3 and 4. Analysis of the $[Co^{I}L_1CO]ClO_4$ crystal structure reveals that five macrocycle carbon atoms exist within ±0.3 Å of the Co–O distance (2.8 Å), which may mask the Ni–O EXAFS component in the analogous Ni complex.

Table IV. EXAFS Results[a–e,h] for Various Ni Complexes at 300 K

complex	N	r, Å (±0.02)	$\Delta\sigma^2$ (±0.001)	ΔE_0	χ^2_{gof}
$[Ni^{II}L_1](ClO_4)_2$	4	1.93	0.0001	0	0.012
$[Ni^{II}L_2](ClO_4)_2$	4	1.94	−0.0001	0	0.011
$[Ni^{II}L_3](ClO_4)_2$	4	1.96	0.0050	0	0.0043
	2	2.17			
$[Ni^{II}L_3](ClO_4)_2$[f]	4	1.88	0.0040	0	0.016
$[Ni^{I}L_1]ClO_4$	4.0*	2.00	0.0062	0	0.013
	2	1.94	0.0019	0	0.015
	2	2.06	0.0012		
	2	1.97	0.0045	5	0.020
	2	2.06	0.0031		
$[Ni^{I}L_2]ClO_4$	4.7*	2.00	0.0086	0	0.0031
	2	1.93	0.0008	0	0.0022
	2	2.08	0.0002		
	2	1.95	0.0008	5	0.0064
	2	2.09	0.0007		
$[Ni^{II}L_3]ClO_4$	4	1.88	−0.0010	0	0.022
$[Ni^{I}L_1CO]ClO_4$	4	2.09	0.0084	0	0.062
	1	1.80	−0.0005		
	2	2.02	−0.0019	0	0.050
	2	2.19	0.0000		
	1	1.80	−0.0031		
$[Ni^{I}L_2CO]ClO_4$	4	2.08	0.0065	0	0.062
	1	1.78	0.0021		
	2	2.01	−0.0018	0	0.050
	2	2.16	−0.0010		
	1	1.78	−0.0005		
$[Ni^{I}L_3CO]ClO_4$[g]	4	2.00	0.0020		0.0015
	1	1.82	−0.0030		

[a] N is the coordination number per nickel. Coordination numbers are based on the X-ray absorption edge spectra and were not varied during optimization except when indicated by *. [b] The nickel-coordinating atom distance (r) is determined from fits of the first-shell EXAFS data. [c] $\Delta\sigma^2$ is a relative mean square deviation in r (the square of the Debye–Waller factor), $\Delta\sigma^2 = \sigma^2_{unknown} - \sigma^2_{std}(NicyclamI_2)$. [d] ΔE_0 is an adjustable parameter related to threshold energy. [e] χ^2_{gof} is a relative goodness-of-fit statistic, defined as $\sum(exp - fit)^2/\sum exp^2$. [f] In CH_3NO_2. [g] In CH_3CN/C_3H_7CN (v/v = 1/5) at 173 K. [h] Experimental details: k range ~ 3.5–10.5, Hanning window = 0.5 $Å^{-1}$, weighting = k^3, R window ~ 0.80–2.0 Å, Hanning window ~ 0.1 Å.

Description of the X-ray Structure of $[NiL_1]ClO_4$. The two nickel atoms in the asymmetric unit are situated on crystallographic inversion centers so that the two halves of the macrocycle are symmetry related. Figure 5 provides a view of unit 1 of the $[Ni^{I}L_1]^+$ cations and atom naming scheme. (The number right after each atom indicates unit 1 or unit 2.) The macrocycle is in the meso form with one amine hydrogen on either side of the plane defined by the nickel and the four nitrogen atoms of the macrocycle. The nickel(I) is coordinated to the four nitrogen atoms of the macrocycle with an average $Ni–N_{amine}$ bond length of 2.066 (6) Å and an $Ni–N_{imine}$ bond length of 1.984 (7) Å. With the macrocycle in the meso form, the axial methyl groups (C17′

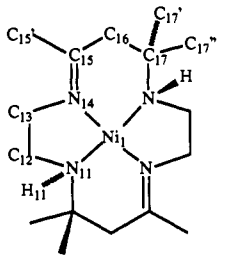

and its inversion atom) essentially block the fifth and sixth coordination sites of the metal center with the Ni–C(axial methyl) distance being 3.33 (1) Å. The amine hydrogens are hydrogen bonded to the perchlorate ion, holding the crystal lattice together and ordering the perchlorate ion.

Optical Spectra. The electronic spectra of $Ni^{I}L_1^+$ and $Ni^{I}L_2^+$ and their CO adducts are shown in Figures S1 and S2 (supplementary material). Although the molar absorptivities for $Ni^{I}L_1^+$ are slightly smaller than those previously reported,[34] the spectrum is quite similar. While the spectra of these species show no dependence upon concentration or temperature, the spectra of $Ni^{II}L_3^+$ anion radical and $Ni^{I}L_3CO^+$ varied dramatically. The spectra of the parent $Ni^{II}L_3^{2+}$ show no dependence upon concentration.

Pronounced UV–vis spectral changes in NiL_3^+ anion radical solutions were observed when the concentration was increased from 3×10^{-5} to 8×10^{-3} M. It has been shown by ESR studies that certain paramagnetic reduced nickel complexes have a tendency to dimerize to form diamagnetic complexes.[16,35] As can be seen in Figure 6 for monomer–dimer mixtures of NiL_3^+, the peak intensity at 1290 nm increases, and the peak intensity at 666 nm decreases as the nickel concentration increases. Upon cooling to −100 °C, all peaks sharpened slightly, but no significant shift of the monomer–dimer equilibrium was observed. In order to estimate K_1 without knowing the molar absorptivities of the monomer and dimer experimentally, we used a treatment established by Schwarz et al.[36–38] where the total absorbance measured at a

$$2Ni^{II}L_3^+(\text{radical}) \rightleftharpoons [Ni^{II}L_3^+]_2 \qquad K_1 \qquad (1)$$

$$A_t = \epsilon_t[Ni]_t = \epsilon_M C_M + 2\epsilon_D C_D \qquad (2)$$

$$[Ni]_t = C_M + 2C_D \qquad (3)$$

$$K_1 = C_D/C_M^2 \qquad (4)$$

given wavelength, A_t, is the sum of monomer and dimer absorbances with the equilibrium concentrations C_M and C_D, respectively, and ϵ_M and ϵ_D the monomer and dimer molar absorptivities, respectively. From eqs 2–4 the following relations were derived

$$[(\epsilon_t - \epsilon_M)/[Ni]_t]^{1/2} = (2K_1/\Delta\epsilon)^{1/2}[\Delta\epsilon - (\epsilon_t - \epsilon_M)] \qquad (5)$$

$$[(\epsilon_M - \epsilon_t)/[Ni]_t]^{1/2} = (2K_1/\Delta\epsilon)^{1/2}[\Delta\epsilon - (\epsilon_M - \epsilon_t)] \qquad (6)$$

When $\epsilon_M < \epsilon_D$, $\Delta\epsilon = \epsilon_D - \epsilon_M$ and eq 5 is used; when $\epsilon_M > \epsilon_D$, $\Delta\epsilon = \epsilon_M - \epsilon_D$ and eq 6 is used. A plot of $[(\epsilon_t - \epsilon_M)/[Ni]_t]^{1/2}$ vs $(\epsilon_t - \epsilon_M)$ (or a plot of $[(\epsilon_M - \epsilon_t)/[Ni]_t]^{1/2}$ vs $(\epsilon_M - \epsilon_t)$) should be linear with intercepts of $(2K_1\Delta\epsilon)^{1/2}$ on the ordinate and $\Delta\epsilon$ on the abscissa. Although the uncertainties associated with K_1 evaluation in this manner are considerable when the monomer and the dimer peaks are overlapping,[38] in our case, the dimer absorption at 1290 nm is well-separated from the monomer absorption at 666 nm. At 1290 nm, we assume that the monomer does not contribute any absorption. Then $\epsilon_t = \epsilon_D$ and $\epsilon_M = 0$ in eq 5. Such a plot is shown on the left-hand side of Figure S3 (supplementary material). The parameters obtained are $\epsilon_D = 5170\ M^{-1}\ cm^{-1}$ at 1290 nm and $K_1 = 6.0 \times 10^3\ M^{-1}$. If we assume $\epsilon_M = 200\ M^{-1}\ cm^{-1}$, $\epsilon_D = 5030\ M^{-1}\ cm^{-1}$ and $K_1 = 5.0 \times 10^3\ M^{-1}$ are obtained. The difference is reasonably small, and the deviation from the least-squares line is slightly better in the first case. Since $\epsilon_M > \epsilon_D$ at 666 nm, we used eq 6 in a similar way. The plot resulting from the 666-nm data with $\epsilon_M = 4000\ M^{-1}\ cm^{-1}$ is shown on the right-hand side of Figure S3. The parameters obtained are $\epsilon_D = 1430\ M^{-1}\ cm^{-1}$ and $K_1 = 5.5 \times 10^3\ M^{-1}$. Among various ϵ_M values tried, this set of parameters gave the smallest deviation and good agreement for K_1. The relatively large deviations of the experimental values are believed to be due to the instability of reduced species toward impurities.

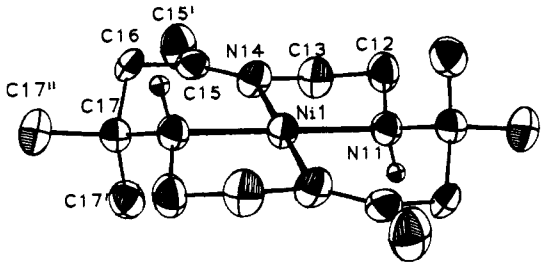

Figure 5. An ORTEP view of a $Ni^{I}L_1^+$ cation. The thermal ellipsoids are at 50% probability level, and the methyl and methylene hydrogen atoms are omitted for clarity. The nickel atom lies on a crystallographic inversion center, and the unlabeled atoms in the macrocycle are related to the labeled atoms by the inversion operation.

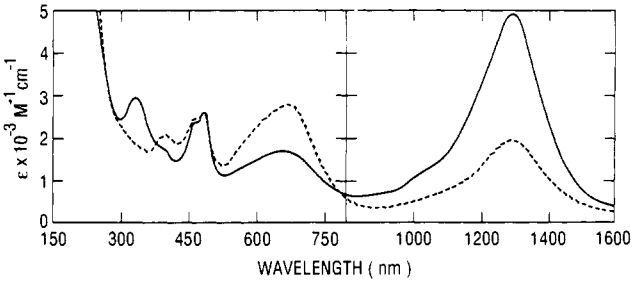

Figure 6. UV–vis spectra of $Ni^{II}L_3^+$ in CH_3CN: broken line, 6.68×10^{-2} mM; solid line, 4.00 mM.

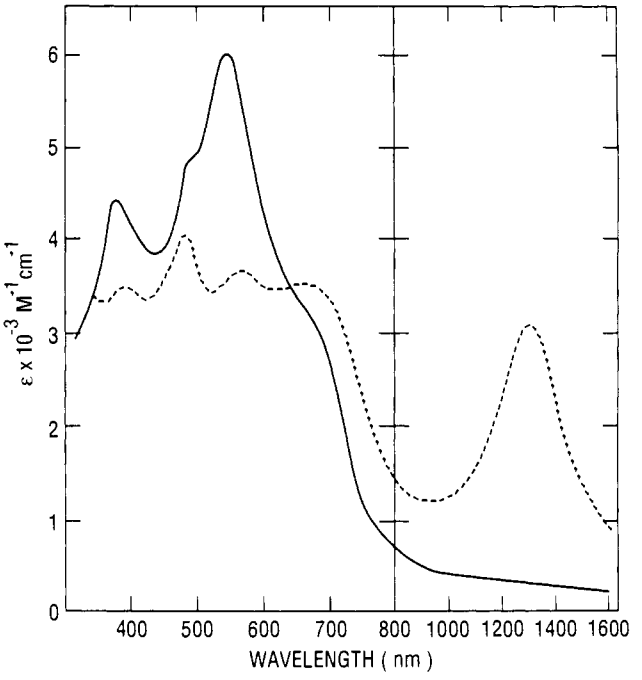

Figure 7. UV–vis spectra of $Ni^{I}L_3CO^+$ in C_3H_7CN under 720 Torr CO: broken line, 300 K; solid line, 153 K.

(34) Olson, D. C.; Vasilevskis, J. *Inorg. Chem.* **1969**, *8*, 1611.
(35) (a) Peng, S.; Ibers, J. A.; Millar, M.; Holm, R. H. *J. Am. Chem. Soc.* **1976**, *98*, 8037. (b) Peng, S.; Goedkin, V. L. *J. Am. Chem. Soc.* **1976**, *98*, 8500.
(36) Schwarz, G.; Klose, S.; Balthasar, W. *Eur. J. Biochem.* **1970**, *12*, 454.
(37) Jennette, K. W.; Gill, J. T.; Sandownick, J. A.; Lippard, S. J. *J. Am. Chem. Soc.* **1976**, *98*, 6159.
(38) Chou, M.; Creutz, C.; Mahajan, D.; Sutin, N.; Zipp, A. P. *Inorg. Chem.* **1982**, *21*, 3989.

Table V. Electronic Absorption Spectra of Nickel Complexes in CH_3CN at 25 °C

macrocycles	λ_{max}, nm (ϵ, M^{-1} cm^{-1})
	Nickel(II) Complexes
L_1	438 (90), 280 (5020), 214 (15 800)
L_2	438 (104), 275 (3760), 222 (23 700)
L_3	415 sh (2240), 396 (2640), 300 sh (820)
L_3[a]	420 sh (2220), 396 (2690), 300 sh (1120)
L_4	400 sh (143), 384 (590), 285 (650)
L_6	460 (20), 230 (2780), 198 (2190)
L_7	445 (42), 195 (8080)
	Nickel(I) Complexes
L_1[b]	600 sh (1270), 468 (4120), 340 sh (2300), 305 (2930)
L_2	600 sh (1230), 458 (3410), 384 (3100), 335 sh (3200), 310 (3400)
L_6	640 (20), 366 (690), 260 sh (800)
L_7	560 (150), 382 (6500), 267 (6300)
	Nickel(I)–CO Adducts
L_1	620 (40), 410 sh (1500), 345 (3600), 301 (3300), 238 (8100)
L_2	610 (120), 420 sh (1500), 330 sh (2900), 297 (3200)
L_3[c]	680 sh (3020), 546 (6000), 480 sh (4710), 400 sh (4100), 378 (4420)
L_6	640 (20), 410 sh (160), 352 (308), 300 sh (160)
L_7	620 (150), 400 sh (1400), 348 (2300)

[a] In C_3H_7CN. [b] The molar absorptivities reported here are slightly smaller than those previously reported in ref 34. [c] In C_3H_7CN at −120 °C.

Table VI. Carbon Monoxide Binding Constants[a] and Carbonyl Vibrational Frequencies for Ni(I) Macrocycles in CH_3CN at 295 K

macrocycle	$E_{1/2}$, V vs SCE	K_{CO}, M^{-1}	ν_{CO}, cm^{-1}
L_3	−0.498	$(1.3 \pm 0.3) \times 10^2$	2012
L_4	−0.823	$(3.7 \pm 0.8) \times 10^2$	1977
L_1	−1.215	$(5.6 \pm 1.5) \times 10^4$	1962
L_2	−1.234	$(1.8 \pm 0.4) \times 10^4$	1961
L_6	−1.243	$(4.0 \pm 1.5) \times 10^4$	1956
L_7	−1.445	$(2.8 \pm 0.6) \times 10^5$	1955

[a] For $Ni^{II}L_3^+$ and $Ni^{II}L_4^+$, K_{CO} is defined the following equation $Ni^{II}L^+ + CO \rightleftharpoons Ni^{I}L\text{–}CO^+$.

Addition of CO to the solution produces a spectral change owing to the formation of the CO adduct as shown in the following eqs 1 and 7. At room temperature in C_3H_7CN under 720 Torr of

$$2Ni^{II}L_3^+(\text{radical}) \rightleftharpoons [Ni^{II}L_3^+]_2 \qquad K_1 \qquad (1)$$

$$Ni^{II}L_3^+(\text{radical}) + CO \rightleftharpoons Ni^{I}L_3CO^+ \qquad K_2 \qquad (7)$$

CO, the optical spectrum indicates the presence of anion-radical monomer, dimer, and the CO adduct of the monomer. Upon cooling to −120 °C, the solubility of CO increases, and the limiting spectrum of NiL_3CO^+ is obtained, see Figure 7. Table V summarizes the optical spectra for the nickel complexes.

Electrochemistry and IR Spectroscopy. Equilibrium constants for CO binding to various nickel macrocycles ([Ni] = 1 mM) in CH_3CN, determined by the electrochemical method, are given in Table VI together with CO vibrational frequencies. These IR results in CH_3CN agree with previously published[15] ν_{CO} in pyridine. The binding constants given for NiL_3^+ and NiL_4^+ are overall equilibrium constants (K_2) with the concentration $[Ni]_t$ = 1 mM.

Discussion

Ni(II) Complexes. The macrocycles L_1 and L_2 studied here have two geometric isomers; N-racemic and N-meso. Both isomers have been characterized by X-ray diffraction and ^1H NMR spectroscopy.[39] The ^1H NMR spectra of our $Ni^{II}L_1^{2+}$ and $Ni^{II}L_2^{2+}$ samples in CD_3CN indicate that the rac isomer (over 90%) is the predominant species at room temperature. Analysis of the EXAFS data for the square-planar, low-spin $Ni^{II}L_1^{2+}$ and

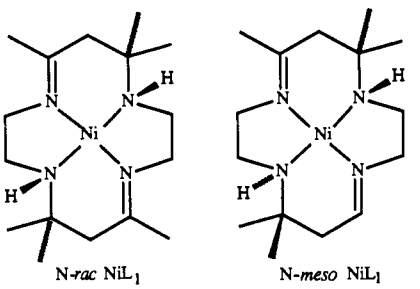

$Ni^{II}L_2^{2+}$ complexes in CH_3CN yields average Ni–N distances of 1.93 (2) and 1.94 (2) Å, respectively, which are slightly longer than those obtained from single-crystal X-ray diffraction data (see Table VII): 1.879 Å for $NiL_1(ClO_4)_2$[29] and 1.909 Å for $Ni^{II}L_2(ClO_4)_2$.[39c] Since the crystal structure of $NiL_1(ClO_4)_2$ was determined from film data (R = 0.12, R_w = 0.16), the reported Ni–N distances may contain larger errors than estimated. The differences between EXAFS and averaged X-ray results of 0.05 Å (for NiL_1^{2+}) and 0.03 Å (for NiL_2^{2+}) are outside our estimated uncertainty of ±0.02 Å. Because of the large discrepancy, we recently redetermined the single-crystal structures of *N-rac*- and *N-meso*-$Ni^{II}L_1(ClO_4)_2$ complexes.[40] The average distances of 1.900 Å in *N-rac*-$Ni^{II}L_1(ClO_4)_2$ and 1.923 Å in *N-meso*-$Ni^{II}L_1(ClO_4)_2$ are in good agreement with the EXAFS data.

The EXAFS results for $Ni^{II}L_3^{2+}$ in CH_3CN of four Ni–N at 1.96 Å and two Ni–N_{ax} at 2.17 Å are consistent with the presence of a high-spin Ni(II) coordinated to two solvent molecules. Although no similar high-spin nickel–imine complex structures have been reported, these distances are quite reasonable. High-spin NiL_7^{2+} complexes have longer Ni–N_{amine} bonds ranging from 2.05 to 2.11 Å and Ni–L_{ax} distances of 2.09–2.56 Å (as shown in Table VII). In contrast, $Ni^{II}L_3^{2+}$ in CH_3NO_2 is low-spin and four-coordinate with a Ni–N_{imine} distance from EXAFS of 1.88 Å. The structure of a nickel complex with a slightly different tetraene ligand (5,7,7,12,12,14-hexamethyl-1,4,8,11-tetraazacyclodeca-4,8,10,14-tetraene) has been determined[41] to have a square-planar geometry with average Ni–N_{imine} distances of 1.885 Å, which agrees with the EXAFS results for NiL_3^{2+}.

Ni(I) and Ni(II) Anion Radical Complexes. The crystals of *meso*-$[Ni^{I}L_1]ClO_4$ were prepared by Na–Hg reduction of the CH_3CN solution of $Ni^{II}L_1(ClO_4)_2$, which is mainly the rac isomer. A conformational change associated with one-electron reduction may have taken place. Alternatively, preferential crystallization of the meso isomer may simply be due to lower relative solubility.

The average Ni–N_{amine} and Ni–N_{imine} bond lengths of 2.066 (6) and 1.984 (7) Å found by X-ray diffraction studies for *meso*-$[Ni^{I}L_1]ClO_4$ are 0.128 and 0.077 Å, respectively, longer than for the *meso*-$Ni^{II}L_1^{2+}$ complex.[40] The large bond length increase can be attributed to the extra electron occupying the $d_{x^2-y^2}$ orbital of the nickel center. Similar effects are noted in high-spin $Ni^{II}L_3^{2+}$, $Ni^{II}L_6^{2+}$, and $Ni^{II}L_7^{2+}$ complexes where the $d_{x^2-y^2}$ orbital is also singly occupied. As seen from Table VII, low-spin Ni(II)–tetraazamacrocycle complexes have Ni–N_{amine} distances of 1.90–1.97 (av 1.941) Å and Ni–N_{imine} distances of 1.85–1.89 (av 1.878) Å. High-spin six-coordinate Ni(II)–tetraazamacrocycle complexes have Ni–N_{amine} distances of 2.05–2.11 (av 2.082) Å, which is 0.14 Å longer than the average Ni–N_{amine} distance of the low-spin complexes. The flexible tetraazacyclotetradeca-4,11-diene ligand can adjust to the large change in core size while conserving the square-planar geometry. Bond distances and bond angles of the ligand in $Ni^{I}L_1^+$ are quite normal.

Reactions involving addition of an electron to a higher energy metal orbital via reduction or a change in spin state can thus induce a metal (Ni) radius change of up to 0.2 Å. In contrast, adding one electron to the half occupied d_{z^2} orbital did not change the structure significantly in the recently reported[17b] structure of the square-planar complex of $[Co^{I}L_5]ClO_4$. The average Co–N_{amine}

(39) (a) Bailey, M. F.; Maxwell, I. E. *J. Chem. Soc. Chem. Commun.* **1966**, 908. (b) Warner, L. G.; Busch, D. H. *J. Am. Chem. Soc.* **1969**, *91*, 4092. (c) Kilbourn, B. T.; Ryan, R. R.; Dunitz, J. D. *J. Chem. Soc. (A)* **1969**, 2407.

(40) Szalda, D. J.; Fujita, E. To be published.

(41) Maxwell, I. E.; Bailey, M. F. *J. Chem. Soc., Chem. Commun.* **1966**, 883.

Table VII. Ni–N and Ni–L_{ax} Bond Distances of Various Ni Macrocyclic Complexes

Ni macrocycle	Ni–N_{amine}, Å	Ni–N_{imine}, Å	Ni–L_{ax}, Å	ref
$[Ni^{II}cyclam Cl_2]ClO_4$	1.974 (3), 1.965 (4), 1.973 (4), 1.963 (4)			55
$[Ni^{III}Me_6cyclam(H_2PO_4)_2]ClO_4$[a]	1.994 (3), 1.994 (3), 2.019 (3), 2.019 (3)		2.048 (3), 2.048 (3)	56
	1.992 (3), 1.992 (3), 2.007 (3), 2.007 (3)		2.074 (3), 2.074 (3)	
$[Ni^{II}cyclam Cl_2]$	2.050 (8), 2.050 (8), 2.066 (8), 2.066 (8)		2.494 (3), 2.492 (3)	57
$[Ni^{II}cyclam(H_2O)_2]Cl_2 \cdot H_2O$	2.092 (2), 2.093 (2), 2.106 (2), 2.109 (2)		2.130 (2), 2.140 (1)	58
$[Ni^{II}Me_6cyclam Cl_2]2CHCl_3$	2.060 (3), 2.060 (3), 2.102 (3), 2.102 (3)		2.562 (1), 2.562 (1)	59
$[Ni^{II}Me_6cyclam F_2]5H_2O$	2.085 (4), 2.085 (4), 2.094 (1), 2.094 (1)		2.087 (1), 2.087 (1)	60
$[Ni^{II}cyclam]I$	1.94 (1), 1.94 (1), 1.96 (1), 1.96 (1)		3.34 (1)	21
$[Ni^{II}cyclam]ZnCl_2$	1.896 (9), 1.896 (9), 1.937 (8), 1.937 (8)			61
$[Ni^{II}(N\text{-}Me)_2cyclam](ClO_4)_2$	1.960 (2), 1.960 (2), 1.973 (2), 1.973 (2)			62
$[Ni^{II}Me_6cyclam]Cl_2 \cdot 2H_2O$	1.957 (1), 1.957 (1), 1.961 (1), 1.961 (1)			59
$[Ni^{II}Me_8cyclam](ClO_4)_2$	1.948 (3), 1.948 (3), 1.961 (2), 1.961 (2)			63
N-rac-$[Ni^{II}L_1](ClO_4)_2$	1.900 (9), 1.904 (9)	1.854 (10), 1.858 (10)		29
N-rac-$[Ni^{II}L_1](ClO_4)_2$	1.914 (4), 1.916 (4)	1.881 (4), 1.887 (5)		40
N-meso-$[Ni^{II}L_1](ClO_4)_2$	1.938 (2), 1.938 (2)	1.907 (2), 1.907 (2)		40
N-rac-$[Ni^{II}L_2](ClO_4)_2$	1.927 (6), 1.927 (6)	1.891 (6), 1.891 (6)		39c
$[Ni^{II}tetraene](ClO_4)_2$		1.881 (9), 1.881 (9), 1.886 (9), 1.886 (9)		41
N-meso-$[Ni^{I}L_1]ClO_4$[a]	2.063 (6), 2.063 (6)	1.988 (7), 1.988 (7)		this work
	2.068 (6), 2.068 (6)	1.979 (7), 1.979 (7)		
Ni^{II}iBC		1.902 (6), 1.910 (7), 1.920 (7), 1.925 (6)		10
Ni^{II}TMiBC		1.908 (3), 1.920 (3), 1.920 (3), 1.926 (3)		64
Ni^{II}oxoporphyrin[a]		1.99 (2), 1.97 (2), 1.97 (2), 1.96 (2)		9a
		2.03 (3), 1.95 (2), 1.95 (2), 1.96 (3)		

[a] The complex has two independent molecules per unit cell.

Table VIII. Co–N and Co–L_{ax} Bond Distances of Various Co Macrocyclic Complexes

Co macrocycle	Co–N_{amine}, Å	Co–N_{imine}, Å	Co–L_{ax}, Å	ref
N-rac-$[Co^{III}L_1(CH_3)(OH_2)](ClO_4)_2$	1.983 (4), 1.983 (4)	1.922 (5), 1.922 (5)	1.971 (6),[a] 2.115 (4)[b]	43a
N-meso-$[Co^{III}L_1(NH_3)_2](ClO_4)_3$	1.986 (6), 1.986 (6)	1.916 (7), 1.916 (7)	1.954 (6), 1.954 (6)	43b
N-rac-$[Co^{II}L_1(OClO_3)]ClO_4$	1.968 (6), 1.965 (5)	1.910 (6), 1.943 (6)	2.305 (5)	42
N-meso-$[Co^{II}L_1Cl_2]$	1.976 (6), 1.976 (6)	1.929 (6), 1.929 (6)	2.747 (2), 2.747 (2)	30
N-meso-$[Co^{I}L_5]ClO_4$[c]	1.961 (11), 1.961 (11)	1.925 (12), 1.925 (12)		17b
	1.952 (12), 1.952 (12)	1.897 (13), 1.897 (13)		
N-rac-$[Co^{I}L_1CO]ClO_4$	2.158 (5), 2.158 (5)	2.075 (5), 2.075 (5)	1.797 (10)	30

[a] Co–CH_3 bond distance. [b] Co–OH_2 bond distance. [c] The complex has two independent molecules per unit cell.

and Co–N_{imine} bond lengths were 1.96 (1) and 1.91 (1) Å, respectively. Although the structure of $[Co^{II}L_5]^{2+}$ has not yet been determined, the structures of *meso*-$[Co^{II}L_1Cl_2]$[30] and *rac*-$[Co^{II}L_1(OClO_3)]ClO_4$[42] were studied. As seen from Table VIII, the Co–N_{amine} and Co–N_{imine} bond distances in these complexes are almost the same as those in $Co^{I}L_5^{+}$. Similarly, the meso versus racemic conformation of the ligand does not affect the metal–N bond length, as observed in $Co^{II}L_1^{2+}$ and $Co^{III}L_1^{3+}$ complexes. Furthermore, in the series of complexes $[CoL_1(CH_3)(OH_2)](ClO_4)_2$,[43a] $[CoL_1(NH_3)_2](ClO_4)_3$,[43b] $[CoL_1Cl_2]$,[30] $[CoL_1(OClO_3)]ClO_4$,[42] and $[CoL_5]ClO_4$,[17b] the coordination geometry varies from octahedral to square-pyramidal to square-planar, and the oxidation state of the metal center from 3+ to 1+, but the Co–N_{amine} and Co–N_{imine} bond lengths do not change significantly.

Analysis of EXAFS data for the reduced species, $Ni^{I}L_1^{+}$ and $Ni^{I}L_2^{+}$, yields two kinds of Ni–N distances (Ni–N_{imine} and Ni–N_{amine}: 1.97 and 2.06 Å for NiL_1^{+}, 1.95 and 2.09 Å for NiL_2^{+}), which show good agreement with the distances obtained from our X-ray diffraction data on NiL_1ClO_4 (Averaged distances of crystallographic independent molecules from X-ray data: 1.984 and 2.066 Å).

The π anion radical of $Ni^{II}L_3^{+}$ undergoes a monomer–dimer equilibrium ($K_1 = 5.5 \times 10^4$ M^{-1}) in CH_3CN as evident from the optical spectrum. However the X-ray absorption edge features show no signs of an axial interaction. Furthermore, the EXAFS showed no obvious evidence for a Ni–Ni interaction, suggesting that the dimer has a long Ni–Ni distance (>2.5 Å) and/or is characterized by a large Debye–Waller factor at room temperature. Indeed reduction of the tetraene ligand to an anion radical does not change the observable geometry around the nickel. On the other hand, reduction of Ni(II) to Ni(I) produces two sets of Ni–N distances which on average are 0.1 Å longer than in the parent Ni(II) complex. This result indicates a distortion in the macrocycle core rather than a simple expansion. The X-ray results support this observation: ΔNi–N = (defined as the difference between Ni–N_{amine} and Ni–N_{imine} distances) 0.031 Å in $Ni^{II}L_1^{2+}$, 0.036 Å in $Ni^{II}L_2^{2+}$, and 0.082 Å in $Ni^{I}L_1^{+}$. Such structural changes associated with ligand versus nickel reduction have also been shown to occur in porphyrin derivatives.[10] The porphyrin results agree well with the results of this study.

A recent conformational analysis[44] of F430 showed that it can easily accommodate both square-planar and, by bending, trigonal-bipyramidal coordination geometries around nickel. It is rather surprising that both Ni(I) and alkyl–Ni(II) species are predicted to adopt the trigonal-bipyramidal geometry. The nickel complexes studied here prefer four-coordinate square-planar and five-coordinate square-pyramidal geometries. Although F430 has a larger core than the macrocycles studied here, consideration of these and other recent experimental results leads us to predict similar geometries for Ni(I) F430. (See Note Added in Proof.)

Monomer–Dimer Equilibrium of $Ni^{II}L_3^{+}$ Anion Radical. ESR and spectroscopic observations have shown that certain paramagnetic nickel d^8 complexes with macrocyclic π cation or π anion ligands have a tendency to dimerize in solution to form diamagnetic adducts.[35,15] The X-ray structures[35] of $Ni^{II}L_8^{+}$ and $Ni^{II}L_9^{+}$ dimers established the diamagnetic modification of cations through intermolecular interactions in the solid state. Ni–Ni metal distances in NiL_8 and NiL_9 dimers are determined to be 2.788 (2) and 3.063 (1) Å, respectively. The solid-state spectrum of NiL_9 shows absorption maxima at 604 nm, in contrast to 560 nm in corresponding solution spectra. However, it has been difficult to quantitate the existence of the equilibrium in the solution. No near-IR spectra of these complexes were reported.

Oligomerization of d^8 complexes is a well-known phenomenon, and the dimerization equilibrium constants of various Rh, Ir, and

(42) Szalda, D. J.; Schwarz, C. L.; Endicott, J. F.; Fujita, E.; Creutz, C. *Inorg. Chem.* **1989**, *28*, 3214.
(43) (a) Heeg, M. J.; Endicott, J. F.; Glick, M. D. **1981**, *20*, 1196. (b) Endicott, J. F.; Durham, B.; Glick, M. D.; Anderson, T. J.; Kuszaj, J. M.; Schmonsees, W. G.; Balakrishnan, K. P. *J. Am. Chem. Soc.* **1981**, *103*, 1431.
(44) Zimmer, M.; Crabtree, R. H. *J. Am. Chem. Soc.* **1990**, *112*, 1062.

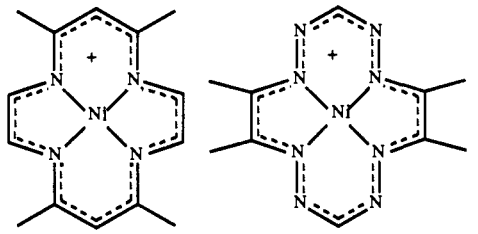

NiL_8^+ NiL_9^+

Pt complexes have been measured.[43-47] The origin of the stability of the oligomers has been considered to be the formation of a weak metal–metal bond and stacking (π–π) interaction between the ligands. Unlike the Rh(I) complex of tetrakis(phenyl isocyanide),[45,46] the HOMO of our nickel monomer ($Ni^{II}L_3^+$ anion radical) is the half-filled ligand π^* orbital, and the absorption at 666 nm may be assigned as LMCT (ligand π^* to metal $d_{x^2-y^2}$). Oligomerization splits the π^* orbitals and lowers the LUMO energy. Thus the absorption of the dimer at 1290 nm may be assigned as a π^*–π^* transition, and the stacking interaction, together with the delocalization of electrons in the LUMO, produces the major stabilization in this dimer. In fact, such dimerization of porphyrins through stacking in the solid state is well-known[48] among neutral porphyrins and their π cations: some examples are the special pair in bacterial reaction centers (from *Rhodopseudomonas viridis*[49a] and *Rhodopseudomonas sphaeroides*[49b,c]), NiTPP,[50] [CuTPP][$SbCl_6$],[51] [ZnTPP]ClO_4,[52] and [ZnOEP(OH_2)]ClO_4.[53] The MgOEP cation radical has been shown[54] to have a monomer–dimer equilibrium constant of (4.7 ± 0.3) × 10^3 M^{-1} in CH_2Cl_2 at 0 °C, which is slightly smaller than that of NiL_3^+ anion radical ((5.5 ± 1.0) × 10^4 M^{-1} at 25 °C). The MgOEP dimer has a lowest absorption at 950 nm, while the monomer absorbs at 670 nm.

CO Adducts. EXAFS data for NiL_1CO^+ and NiL_2CO^+ clearly indicate that these are five-coordinate complexes with short Ni–C bonds of 1.80 and 1.78 Å, respectively. Both Ni–N distances in the CO adducts increase quite dramatically (2.02 and 2.19 Å for NiL_1, 2.01 and 2.16 Å for NiL_2) and further distortion in the macrocycle core is indicated. The X-ray structure[30] of [$Co^{I}L_1$-CO]ClO_4 (Co–C 1.797 Å, Co–N_{imine} 2.075 Å, Co–N_{amine} 2.158 Å, with Co 0.57 Å above the plane of the coordinating nitrogen atoms) supports this trend: ΔCo–N 0.083 Å in this compound versus 0.040 Å in [$Co^{II}L_1(OClO_3)$]ClO_4. By analogy with the cobalt(I)–CO complex the nickel atom must be situated above the plane of four nitrogens. These structural results are consistent with previously reported ESR results for NiL_1CO^+ and NiL_2CO^+, which show rhombic distortions upon coordination of CO.[15]

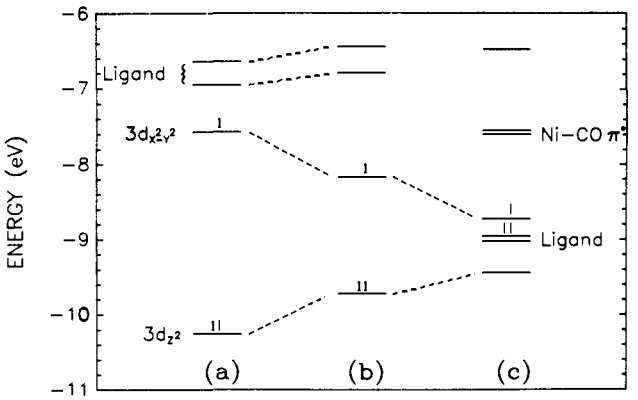

Figure 8. Extended Hückel energies of the NiL_1 complex: (a) $Ni^{I}L_1^+$ energies with $Ni^{II}L_1^{2+}$ structure, (b) $Ni^{I}L_1^+$ energies with $Ni^{I}L_1^+$ structure, (c) $Ni^{I}L_1CO^+$ energies with $Co^{I}L_1CO^+$ structure.

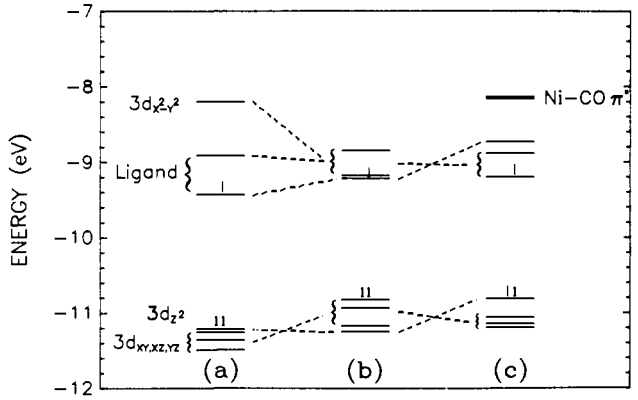

Figure 9. Extended Hückel energies of the NiL_3 complex: (a) $Ni^{II}L_3^+$ energies with $Co^{II}L_3^{2+}$ structure, (b) same as (a) except Ni was placed 0.57 Å out of the plane of four nitrogens, (c) $Ni^{I}L_3CO^+$ energies with CO placed in the structure of (b) with Ni–C = 1.82 Å.

Previous ESR results[15] have also shown that coordination of CO to the $Ni^{II}L_3^+$ anion radical in propylene carbonate glass at 100 K yields a Ni(I) signal with axial symmetry. The EXAFS results at 173 K show a short Ni–CO bond of 1.82 Å and four equal Ni–N bonds of 2.00 Å, consistent with a five-coordinate Ni situated symmetrically above the nitrogen plane. The average Ni–N distances differ significantly from those of NiL_1CO^+ and NiL_2CO^+.

As can be seen from Table VI, CO stretching frequencies decrease, and CO binding constants increase as NiL^+ becomes a more powerful reductant. This trend is consistent with the backbonding interaction in the binding of CO to nickel. Gagné et al. reported[15] CO binding constants in DMF and carbonyl vibrational frequencies in pyridine: NiL_3^+, K_{CO} = 1.7 × 10^2 M^{-1}, ν_{CO} = 2020 cm^{-1}; NiL_2^+, 1.8 × 10^4 M^{-1}, 1957 cm^{-1}; NiL_1^+, 4.7 × 10^4 M^{-1}, 1962 cm^{-1}; NiL_6^+, 7.8 × 10^4 M^{-1}, 1949 cm^{-1}. The CO binding constants and CO vibrational frequencies are very similar for CH_3CN, DMF, and pyridine. It was suggested that the predominant interaction in CO binding is σ interaction with the metal 4s and 4p orbitals because of the lack of dependence of the carbonyl stretching frequency on K_{CO} for the various nickel complexes studied. Cobalt(I) complexes of similar ligands show stronger CO binding:[17b] CoL_3^+, K_{CO} = 5 × 10^4 M^{-1}, ν_{CO} = 2007 cm^{-1}; CoL_4^+, 1.4 × 10^4 M^{-1}, 1957 cm^{-1}; CoL_2^+, 1.9 × 10^8 M^{-1},

(45) Mann, K. R.; Gordon, J. G., II.; Gray, H. B. *J. Am. Chem. Soc.* **1975**, *97*, 3553.
(46) Mann, K. R.; Lewis, N. S.; WIlliams, R. M.; Gray, H. B.; Gordon, J. G., II. *Inorg. Chem.* **1978**, *17*, 828.
(47) Geoffroy, G. L.; Bradley, M. G.; Keeney, M. E. *Inorg. Chem.* **1978**, *17*, 777.
(48) Scheidt, W. R.; Lee, Y. J. *Struct. Bonding (Berlin)* **1987**, *64*, 1 and references cited therein.
(49) (a) Deisenhofer, J.; Epp, O.; Miki, K.; Huber, R.; Michel, H. *J. Mol. Biol.* **1984**, *180*, 385. (b) Chang, C.-H.; Tiede, D.; Tang, J.; Smith, U.; Norris, J.; Schiffer, M. *FEBS Lett.* **1986**, *205*, 82. (c) Allen, J. P.; Feher, G.; Yeates, T. O.; Komiya, H.; Rees, D. C. *Proc. Natl. Acad. Sci. U.S.A.* **1987**, *84*, 5730.
(50) Brennan, T. D.; Scheidt, W. R.; Shelnutt, J. A. *J. Am. Chem. Soc.* **1988**, *110*, 3919.
(51) Scholz, W. F.; Reed, C. A.; Lee, Y. L.; Scheidt, W. R.; Lang, G. *J. Am. Chem. Soc.* **1982**, *104*, 6791.
(52) Barkigia, K. M.; Spaulding, L. D.; Fajer, J. *Inorg. Chem.* **1982**, *22*, 349.
(53) Song, H.; Reed, C. A.; Scheidt, W. R. *J. Am. Chem. Soc.* **1989**, *111*, 6867.
(54) Fajer, J.; Borg, D. C.; Forman, A.; Dolphin, D.; Felton, R. H. *J. Am. Chem. Soc.* **1970**, *92*, 3451.
(55) Ito, T.; Sugimoto, M.; Toriumi, K.; Ito, H. *Chem. Lett.* **1981**, 1477.
(56) Zeigerson, E.; Bar, I.; Bernstein, J.; Kirschenbaum, L. J.; Mayerstein, D. *Inorg. Chem.* **1882**, *21*, 73.
(57) Bosnich, B.; Mason, R.; Pauling, P. J.; Robertson, G. B.; Tobe, M. L. *J. Chem. Soc., Chem. Commun.* **1965**, 97.
(58) Emsley, J.; Arif, M.; Bates, P. A.; Hursthouse, M. B. *J. Chem. Soc., Chem. Commun*, **1988**, 1387.
(59) Ito, T.; Toriumi, K. *Acta Crystallogr.* **1981**, *B37*, 88.
(60) Toriumi, K.; Ito, T. *Acta Crystallogr.* **1981**, *B37*, 240.
(61) Barefield, E. K.; Bianchi, A.; Billo, E. J.; Connolly, P. J.; Paoletti, P.; Summers, J. S.; Van Derveer, D. G. *Inorg. Chem.* **1986**, *25*, 4197.
(62) Miyamura, K.; Kohzuki, M.; Narushima, R.; Saburi, M.; Gohshi, Y.; Tsuboyama, S.; Tsuboyama, K.; Sakurai, T. *J. Chem. Soc., Dalton Trans.* **1987**, 3093.
(63) Ferguson, G.; Lough, A. J. *Acta Crystallogr.* **1990**, *C46*, 213.
(64) Suh, M. P.; Swepston, P. N.; Ibers, J. A. *J. Am. Chem. Soc.* **1984**, *106*, 5164.

1918 cm^{-1}; CoL_1^+, 2.3×10^8 M^{-1}, 1916 cm^{-1}. The large CO binding constants and lower carbonyl vibrational frequencies suggest stronger metal(I)-to-CO backdonation in the corresponding cobalt complexes.

Theoretical Calculations. Extended Hückel calculations were carried out to elucidate the factors which govern the site of reduction, the distortions evident upon formation of Ni(I), and why the electron migrates from the macrocycle to the metal upon coordination of CO in NiL_3^+. Computations based on the published X-ray coordinates for $Ni^{II}L_1$ and $Ni^{II}L_3$ with an additional electron reveal that the HOMO in the former case is the metal $d_{x^2-y^2}$ orbital and in the latter a ligand π^* orbital (see Figures 8a and 9a). The presence of a conjugated system apparently provides two ligand orbitals (π^*) below the unoccupied metal orbital ($d_{x^2-y^2}$). This also explains why a conjugated diene complex, $Ni^{II}L_4$, forms an anion radical upon reduction.[14]

In order to understand the core distortions found in the Ni(I) complexes, computations were made to compare the $Ni^{I}L_1$ structure (Figure 8b) with the $Ni^{II}L_1$ structure (Figure 8a) containing an additional electron. The half occupied HOMO ($d_{x^2-y^2}$) is lower in energy in the distorted structure, though the total energies are largely unchanged. More sophisticated MO calculations are probably needed to fully explain the stabilizing effect. The $d_{x^2-y^2}$ HOMO orbital is further stabilized upon the coordination of CO (Figure 8c) and the concomitant out-of-plane shift of the metal.

The binding of CO to $Ni^{II}L_3^+$ was modeled with an unperturbed tetraene ligand, the Ni 0.57 Å out of the four-nitrogen plane, and our experimentally determined Ni–CO bond length (Figure 9c). The HOMO has in this case acquired substantial $d_{x^2-y^2}$ character. This transfer of the electron from the ligand to the metal is largely due to the out-of-plane displacement of the nickel, as shown in Figure 9b, where the relative $d_{x^2-y^2}$ orbital stabilization is evident even without the binding of CO. This is consistent with ESR results for reduced Ni porphyrins[9e] in DMF, which suggest an out-of-plane displacement.

Conclusions

The results of the present study clearly illustrate the utility of EXAFS techniques for the study of structural changes associated with redox reactions in solution. The two Ni(I)–tetraazamacrocycle complexes investigated here both display the distorted core environment suggested for Ni^{I}iBC.[10] The crystal structure of $[Ni^{I}L_1]ClO_4$ verified these results and is the first reported Ni(I) structure with all nitrogen ligands. Though the source of the distortions is not fully understood, the Hückel calculations show a stabilizing effect on the $d_{x^2-y^2}$ orbital. We expect similar distortions to occur in F430 upon reduction. (See Note Added in Proof.)

The CO adducts of $Ni^{I}L_1^+$ and $Ni^{I}L_2^+$ were found to have short Ni–C bonds, similar to the corresponding cobalt complexes, but with significantly weaker metal to CO backbonding. The coordination of CO to $Ni^{II}L_3^+$ (anion radical) to form $Ni^{I}L_3CO^+$ was shown to involve a substantial displacement of the metal out of the four-nitrogen plane. The Hückel calculations show that this is an alternate route toward Ni(I) formation.

Nickel(I) F430,[6] hydroporphyrin,[9d] and tetraazamacrocyclic[16] complexes all show reactivity toward alkyl halides to produce alkanes and/or other related products. Proposed reaction mechanisms typically involved the formation of a Ni^{II}–C bond. The newly developed anaerobic techniques should allow structural studies of these highly reactive intermediates at low temperature and may provide insight into the carbon–sulfur bond cleavage of *S*-methyl coenzyme M as mediated by F430 in the enzymatic process.

Note Added in Proof. Subsequent to this work, EXAFS measurements on Ni(I) F430M confirmed the formation of a similarly distorted macrocyclic core. (Furenlid, L. R.; Renner, M. W.; Fajer, J. *J. Am. Chem. Soc.* **1990**, *112*, 8987.)

Acknowledgment. We thank Drs. Carol Creutz, Jack Fajer, and Marshall Newton for helpful discussions and E. Norton for performing analyses for nickel and ClO_4^-. This research was carried out at Brookhaven National Laboratory under contract DE-AC02-76CH00016 with the U.S. Department of Energy and supported by its Division of Chemical Sciences, Office of Basic Energy Sciences. EXAFS experiments were performed at Beam Line X-9A of the National Synchrotron Light Source at BNL. X-9A is operated by the National Biostructures PRT with support from NIH Grant PR01633.

Supplementary Material Available: Tables of crystallographic data collection parameters, final positional parameters for the non-hydrogen atoms, anisotropic thermal parameters for non-hydrogen atoms, calculated hydrogen atom positions, bond distances and angles, and hydrogen-bonding parameters, figures of optical spectra of NiL_1^+ and NiL_1CO^+ and NiL_2^+ and NiL_2CO^+, and determination of dimerization constant for $Ni^{II}L_3^+$ (12 pages); table of observed and calculated structure factors (9 pages). Ordering information is given on any current masthead page.